ACS Catalysis

Research Article

Cite This: ACS Catal. 2018, 8, 2209−2217

pubs.acs.org/acscatalysis

# Consciously Constructing Heterojunction or Direct Z-Scheme Photocatalysts by Regulating Electron Flow Direction

Wenshuai Jiang,[†] Xupeng Zong,[‡,§] Li An,[†] Shixin Hua,[†] Xiang Miao,[‡,§] Shiliang Luan,[†] Yuanjing Wen,[†] Franklin Feng Tao,[∥] and Zaicheng Sun*[,†]

[†]Beijing Key Laboratory for Green Catalysis and Separation and Department of Chemistry and Chemical Engineering, College of Environmental and Energy Engineering, Beijing University of Technology, Beijing 100124, People's Republic of China

[‡]State Key Laboratory of Luminescence and Application, Changchun Institute of Optics, Fine Mechanics and Physics, CAS, Changchun 100033, People's Republic of China

[§]University of Chinese Academy of Sciences, Beijing 100000, People's Republic of China

[∥]Department of Chemical and Petroleum Engineering, Department of Chemistry, University of Kansas, Lawrence Kansas 66047, United States

Supporting Information

**ABSTRACT:** Heterojunction and direct Z-scheme nanostructures are two typical representatives of an efficient photocatalyst, which is composed of two semiconductors. However, it is a great challenge to construct each of them on purpose. The photodeposition technique can be a potentially powerful tool to regulate the electron flow direction for constructing these nanostructures. In this report, CdS nanoparticles were deposited on the g-$C_3N_4$ nanosheets by photodeposition and chemical deposition methods for comparison. In the photodeposition case, PL and charge flow tracking demonstrate that a type II heterojunction is constructed because CdS is selectively deposited at the electron transfer site of g-$C_3N_4$, which leads to the photoexcited electron from g_$C_3N_4$ tending to transfer to CdS in the composites. In the latter, the CdS is randomly deposited onto the g-$C_3N_4$ nanosheets through chemical deposition. There is no preferred site for deposition or charge transfer in the composite. The results illustrate that the electron of CdS tends to recombine with the hole from g-$C_3N_4$. The direct Z-scheme is predominant for the CdS/g-$C_3N_4$ prepared by the chemical deposition route. Furthermore, the photocatalytic performance and stability also confirm the above results. On the of these, we can deduce that the photodeposition method can be used to regulating the electron transfer route. We expect this report to shed light on the rational design of heterojunction or direct Z-scheme type composites.

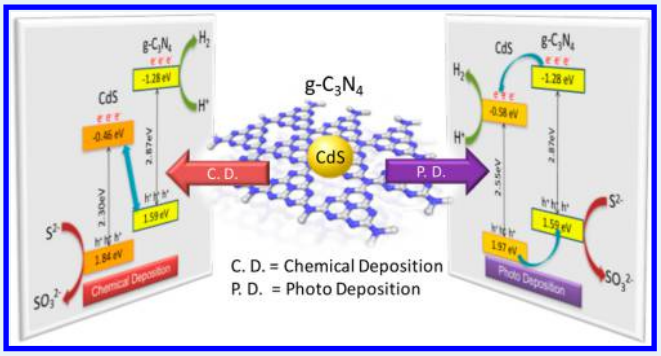


**KEYWORDS:** *type II heterojunction, direct Z-scheme, photodeposition, CdS, g-$C_3N_4$, composite photocatalyst*

## INTRODUCTION

Photocatalytic water splitting has attracted substantial attention as a potential system for clean hydrogen energy.[1−3] To utilize solar energy efficiently, photocatalysts are highly expected to possess broadly visible light adsorption and high charge separation efficiency.[4−9] Currently, single-photocatalyst systems, such as $TiO_2$, g-$C_3N_4$, and sulfide compounds, hardly satisfy these requirements for full-spectrum water splitting.[10,11] Constructing composite materials has been put forward to further broaden the light adsorption and enhance the charge separation of the photocatalyst.[12,13] A heterojunction forms at the interface between two semiconductors with unequal band gaps by physical contact with each other. In a type II heterojunction, the excited electrons and holes kinetically flow downward and upward, respectively.[14] This leads to the electron and hole spatial separation and enhances the charge separation efficiency. A Z-scheme type photocatalyst is another composite system for water splitting to mimic the natural photosynthesis process, in which the excited electron of photosystem II (PSII) is transferred toward photosystem I (PSI) and recombined with the hole on it with the aid of an electron-transfer mediator. The excited electrons of PSI and the holes of PSII with high reduction and oxidation capability are left and used for reduction and oxidation reactions.[15,16] The electron mediators could be ionic type redox pairs such as $IO_3^-/I^-$, $Fe^{3+/2+}$, and $Co(bpy)_3^{3+/2+}$ or conductor-like metal nanoparticles and reduced graphene oxide (RGO).[17−25] Recently, a new type of Z-scheme system without any redox mediator was proposed and called a direct Z-scheme.[26−28] Two semiconductors are placed together just as for a type II

Received: December 16, 2017
Revised: January 23, 2018
Published: February 2, 2018






DOI: 10.1021/acscatal.7b04323
ACS Catal. 2018, 8, 2209−2217

heterojunction; however, the charge transfer route follows the Z-scheme, in which the excited electron of one semiconductor recombines with the hole of another semiconductor in the direct Z-scheme. Notably, the backward reactions and the shielding effect of a Z-scheme system with redox mediators are primarily suppressed because of the absence of redox mediators.[25]

Bewilderingly, both type II heterojunction and direct Z-scheme catalysts are composed by simply contacting two semiconductors together. Until now, it is still an open question and challenge to consciously construct type II heterojunction and/or direct Z-scheme catalysts. Photodeposition is a common method to deposit the cocatalyst Pt onto a catalyst to enhance the electron transfer toward Pt nanoparticles.[29] Thus, the photodeposition technique could be used to regulate the electron transfer direction. Thus, we proposed constructing these two systems by regulating excited electron flow direction, since they have different electron transfer routes. To prove this concept, we synthesized CdS/g-$C_3N_4$ composites by a photodeposition route. For comparison, CdS/g-$C_3N_4$ composites were also synthesized via a chemical deposition route. In the case of Photodeposition, CdS was selectively formed on the site, where the photo excited electron prefers transferring to, because the sulfur was reduced to form sulfide at the same site. Thus, the photoexcited electron of g-$C_3N_4$ prefers to be transferred to CdS in the CdS/g-$C_3N_4$ composite. The PL and electron flow tracking experiment results confirm the formation of a type II heterojunction in the composites. In the case of chemical deposition, CdS was randomly deposited onto the g-$C_3N_4$ nanosheets in the chemical deposition. There is no preference for photogenerated electron transfer. The PL and charge flow tracking experiment results indicate that the direct Z-scheme type takes a dominant place in this composite. The photocatalytic performance and stability further demonstrate that the holes are transferred from CdS to g-$C_3N_4$, which effectively prevent CdS from photocorrosion, in the composites prepared via the photodeposition route. On the other hand, the recombination takes place between an electron from CdS and a hole from g-$C_3N_4$ in the direct Z-scheme type composite. The hole left at CdS potentially oxidizes the catalyst and deteriorates the performance of the catalyst. This report opens the door to the rational design of type II heterojunction and/or Z-scheme catalysts by controlling the electron flow direction using different synthesis routes.

## RESULTS AND DISCUSSION

Typically, g-$C_3N_4$ nanosheets were prepared through the pyrolysis of urea.[30] Photodeposition of CdS onto g-$C_3N_4$ nanosheets (p-CSCN) was synthesized in an ethanol dispersion of 0.2 g of g-$C_3N_4$ containing 2 mmol of S powder and 8 mmol of $Cd(NO_3)_2$; the deposition temperature was set at 4, 25, and 50 °C for 2 h to obtain p-CSCN-4, -25, and -50, respectively.[31] The S first was photoreduced into $S^{2-}$ under light irradiation by g-$C_3N_4$. CdS immediately forms at the $S^{2-}$ site due to the presence of excess $Cd^{2+}$. The chemical deposition of CdS/g-$C_3N_4$ composites (c-CSCN) was achieved by a hydrothermal route[32] by adding 0.5 g of g-$C_3N_4$ to a $Cd(NO_3)_2$ and thioacetamide (TAA) aqueous solution at 160 °C for 5 h. The amount of CdS was tuned by $Cd(NO_3)_2$ from 0.035 to 0.525 mmol to obtain c-CSCN-1−15% samples. After optimization (Figures S1−S5 in the Supporting Information), p-CSCN-25 and c-CSCN-10% were chosen as typical samples for further comparative investigation of p-CSCN and c-CSCN.

Figure 1 shows typical scanning electron microscopy (SEM) and TEM images of g-$C_3N_4$, p-CSCN-25, and c-CSCN-10%

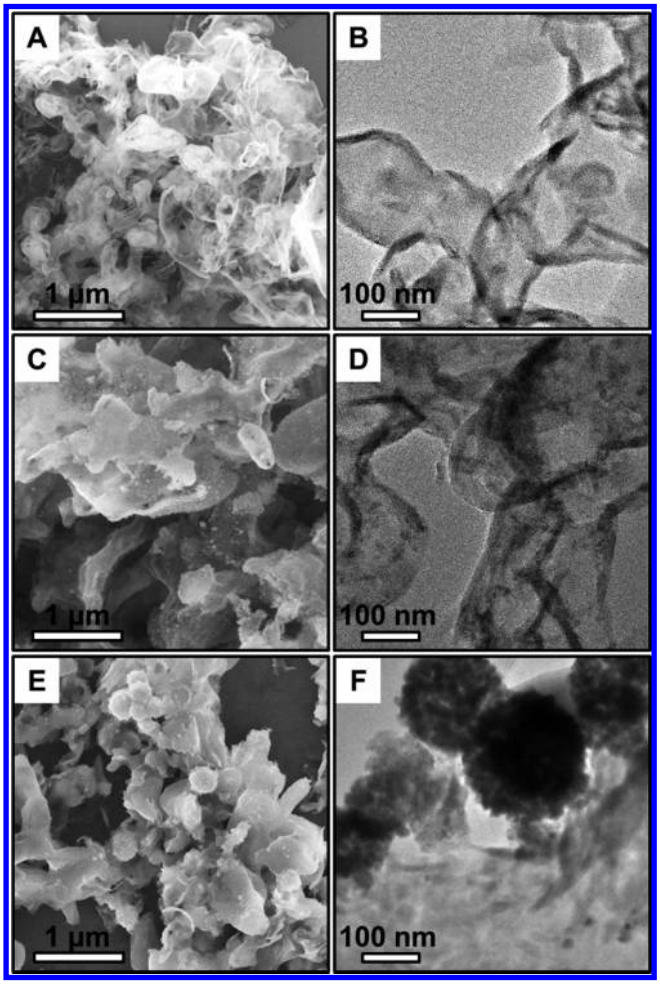


**Figure 1.** Morphologies of g-$C_3N_4$, p-CSCN-25, and c-CSCN-10% samples: scanning electron microscopy (SEM) and transmission electron microscopy (TEM) images of g-$C_3N_4$ (A, B), p-CSCN-25 (C, D), and c-CSCN-10% (E, F).

photocatalyst composites. g-$C_3N_4$ exhibits a nanosheet morphology with a high specific surface area (~93 $m^2$ $g^{-1}$, Figure S6 and Table S1). The specific surface areas slightly decrease to 76 $m^2$ $g^{-1}$ after loading of CdS due to the stacking of nanosheets. In the case of p-CSCN-25, CdS nanoparticles were individually deposited on the surface of g-$C_3N_4$ (Figure 1C). The TEM image displays CdS nanoparticles of ~4.0 nm average size on the g-$C_3N_4$ nanosheets, resulting in CdS having a relatively large band gap and narrow visible light adsorption.[33] Figure 1E,F presents the SEM and TEM images of c-CSCN-10%, which show many large spherical nanoparticle aggregates (~200 nm in diameter) on the surface of g-$C_3N_4$ in addition to small particles with a size of ~20 nm. SEM images of c-CSCN series samples, as shown in Figure S7, disclose that most of the CdS nanoparticles tend to separately scatter on the surface when the amount of CdS is low (~1%). However, CdS nanoparticles tend to aggregate and form large spheres on overloading. This may be the reason the photocatalytic performance of c-CSCN-15% is lower than that of c-CSCN-10%.



DOI: 10.1021/acscatal.7b04323
ACS Catal. 2018, 8, 2209−2217

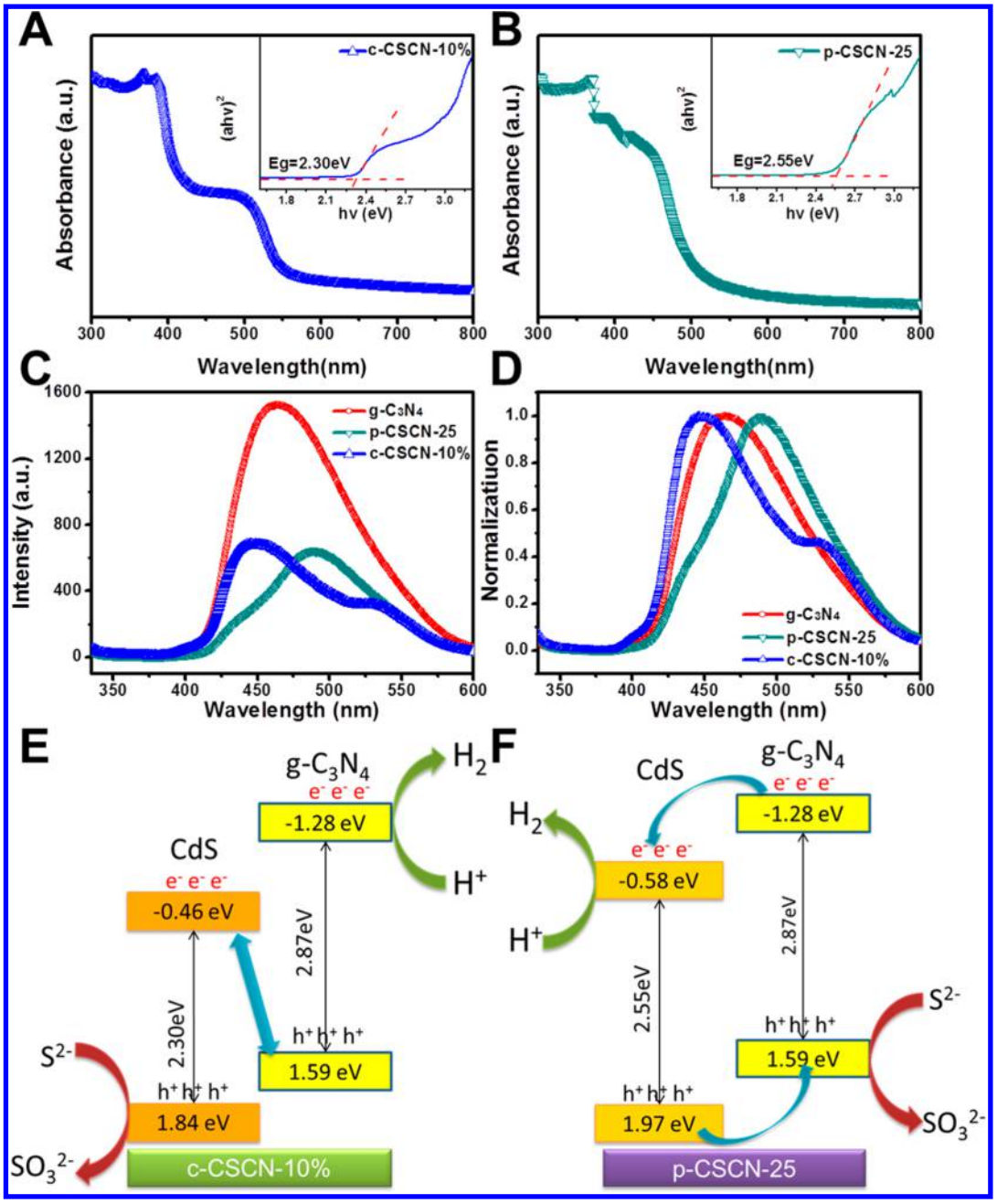


**Figure 2.** Optical properties of CSCN composites. UV−vis spectra and Tauc plots of $(\alpha h\upsilon)^2$ vs photon energy for band gap calculations of c-CSCN-10% (A) and p-CSCN-25 (B). Photoluminescence (PL, C) and normalized PL (D) spectra of g-$C_3N_4$, c-CSCN, and p-CSCN. Energy level diagrams and charge transfer routes of c-CSCN-10% (E) and p-CSCN-25 (F).

To prove our concept, the energy level diagram was calculated and measured. From the UV−vis spectra of g-$C_3N_4$, CdS, and CdS/g-$C_3N_4$ composite (Figure S2), the optical band gap can be obtained from a transformed Kubelka−Munk function (Figure 2A,B insets): 2.87 eV for g-$C_3N_4$, 2.30 eV for CdS in c-CSCN, and 2.58 eV for CdS in p-CSCN, respectively. In general, the CB and VB band edge positions of a semiconductor can be determined using a simple method.[34,35] The conduction band (CB) edge of a semiconductor at zero charge can be determined using the equation

$$E_{CB} = \chi - E^e - 1/2E_g \quad (1)$$

$$E_{VB} = E_g + E_{CB} \quad (2)$$

where $E_{CB}$ is the CB edge potential, $E_{VB}$ is the valence band (VB) edge potential, and $\chi$ is the electronegativity of the semiconductor, expressed as the geometric mean of the absolute electronegativity of the constituent atoms, which is defined as the arithmetic mean of the atomic electron affinity and the first ionization energy. $E^e$ is the energy of free electrons on the hydrogen scale, ∼4.5 eV, and $E_g$ is the band gap of the semiconductor. According to the band gap of g-$C_3N_4$ of 2.87 eV, the calculated CB and VB of g-$C_3N_4$ are −1.28 and 1.59 eV vs NHE, respectively, which are close to those in Wang's report.[36] The band gaps of CdS in c-CSCN and p-CSCN are 2.30 and 2.58 eV, respectively. The calculated CB and VB are −0.46 and 1.84 eV for CdS in c-CSCN and −0.58 and 1.97 eV for CdS in p-CSCN. In addition, valence band X-ray



DOI: 10.1021/acscatal.7b04323
ACS Catal. 2018, 8, 2209−2217

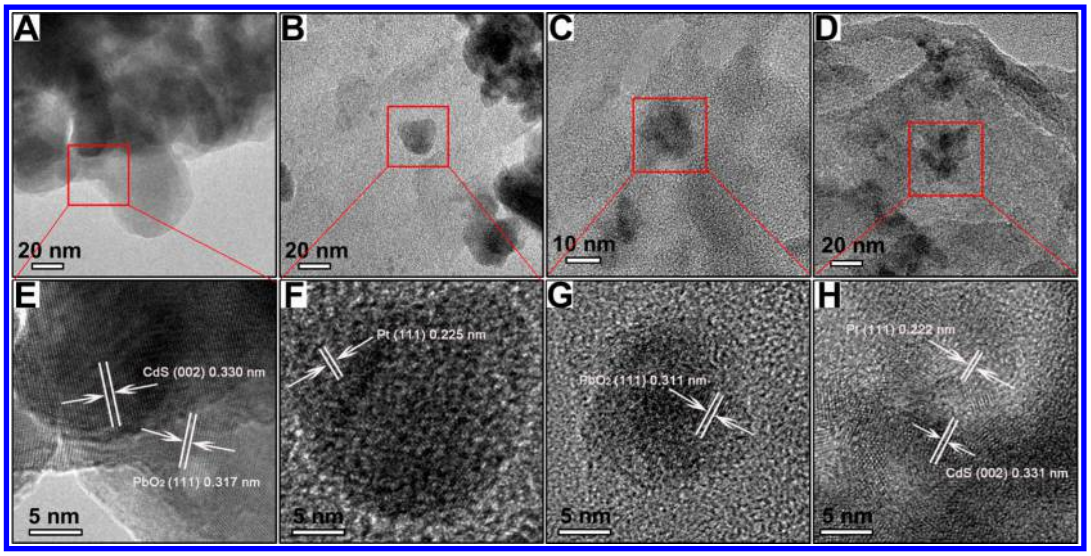


**Figure 3.** Charge transfer route of c-CSCN-10% and p-CSCN-25. TEM images of c-CSCN-10% (A, B, E, F) and p-CSCN-25 (C, D, G, H) photodeposited with $PbO_2$ nanoparticles (A, E, C, G) and Pt (B, F, D, H) nanoparticles. (E−H) give the corresponding high-resolution TEM images, respectively.

photoelectron spectroscopy (VB XPS) has been employed to verify the position of VB of the catalysts. Figure S3 illustrates the VB XPS spectra of g-$C_3N_4$, p-CSCN-25, and c-CSCN-10%. The VB of g-$C_3N_4$ is 1.49 eV, which is close to the calculated value. The VB of p-CSCN-25 is 1.55 eV, which is close to the VB of g-$C_3N_4$. This indicates that the holes rapidly transfer from CdS to g-$C_3N_4$. The VB of c-CSCN-10% is 1.79 eV, which is close to the VB of CdS. This implies that the holes are left on the CdS in c-CSCN. On the basis of these results, the energy level diagram of CdS/g-$C_3N_4$ and the charge transfer route are proposed and shown in Figure 2E,F.

Photoluminescence (PL) spectroscopy has been employed to characterize the charge transfer of CdS/g-$C_3N_4$ composites. As shown in Figure 2C, the PL intensity greatly decreases, indicating that the radiation recombination of g-$C_3N_4$ is depressed and charge separation is enhanced because of the formation of both Z-scheme and type II heterojunctions in the CdS/g-$C_3N$ composite. g-$C_3N_4$ shows a PL emission peak at ~464 nm (2.67 eV), which is smaller than the optical band gap of g-$C_3N_4$ (2.87 eV), in which the relaxation of an excited electron from the bottom of the CB to the sub-band (or surface state) and the radiative transition from the sub-band to the top of the VB subsequently lead to PL emission. In the case of c-CSCN, the maximum emission has a blue shift from ~464 to ~443 nm (2.80 eV), indicating that a new radiation recombination happens as in g-$C_3N_4$. The corresponding transition (2.80 eV) is about 0.13 eV greater than that of g-$C_3N_4$, indicating that the emission transition is not from pure g-$C_3N_4$. According to Yan's report, P3HT/g-$C_3N_4$ composites exhibited two new PL emission peaks at 375 and 720−750 nm in addition to emission from the individual g-$C_3N_4$ and P3HT. They assigned these two new PL emissions as the transition from the excited electron of P3HT with the hole of g-$C_3N_4$ and the recombination of the excited electron of g-$C_3N_4$ with the hole of P3HT.[37−39] Zhou et al. also reported an indirect optical transition effect in the multilayer $Ti_{0.91}O_2$/CdS hollow spheres. PL spectra disclosed the recombination between the excited electron of $Ti_{0.91}O_2$ and the hole of CdS via d−p conjugation.[25,40] Thus, we believe that the emission at 443 nm mainly comes from the recombination of the excited electron of g-$C_3N_4$ with the hole from CdS. The emission at 525 nm is contributed by CdS. In the case of p-CSCN, there should be a peak at 440 nm and a red-shifted emission peak at 485 nm (Figure 2D). The former may be minor recombination, similar to the emission at 443 nm in c-CSCN. The major emission at 488 nm (2.52 eV) can be attributed to the transition from the CB to VB of CdS because it is close to the band gap (2.58 eV) of CdS. This transition contains not only an excited electron from CdS but also an excited electron transferred from g-$C_3N_4$. On the basis of PL results, we speculate the nature of the charge transfer route is as shown in Figure 2E,F.

To confirm the charge transfer route, the photodeposition of Pt and $PbO_2$ nanoparticles was carried out for both c-CSCN and p-CSCN. Generally, Pt nanoparticles, reduced from $H_2PtCl_6$ by acceptance of an electron, can be used for characterization of the site of photogenerated electron flow, and $PbO_2$, oxidized from $Pb(NO_3)_2$ by accepting hole, characterizes the hole transfer route.[41] Figure 3A,E illustrate the TEM images of photodeposition of $PbO_2$ nanoparticles on c-CSCN. Figure 3E clearly exhibits that two connected particles with lattice fringe spacings of 0.330 and 0.317 nm are observed in the HR TEM images. They are assigned to the (002) plane of CdS and (111) plane of $PbO_2$, indicating that the $PbO_2$ nanoparticles were photodeposited onto the CdS particles. This implies hole transfer from CdS to $PbO_2$. Figure 3B,F gives the TEM images of Pt nanoparticle deposition. The HR TEM images show that the lattice fringe space is 0.225 nm, corresponding to the (111) plane of Pt. Also, there are no other particles surrounding the Pt nanoparticles, indicating that the Pt nanoparticles were directly deposited onto g-$C_3N_4$. This implies that the electron transfers from g-$C_3N_4$ to Pt nanoparticles. These results illustrate that the photogenerated electron remains at g-$C_3N_4$ and hole tends to be located at the site of CdS in c-CSCN-10% sample.

Figure 3C,D gives TEM images of the corresponding photodepositions of Pt and $PbO_2$ on p-CSCN-25. $PbO_2$ nanoparticles with a lattice fringe spacing of 0.311 nm were observed and existed separately on the g-$C_3N_4$ surface (Figure 3C,G). This implies that the hole transfers from g-$C_3N_4$ to the


DOI: 10.1021/acscatal.7b04323
ACS Catal. 2018, 8, 2209−2217

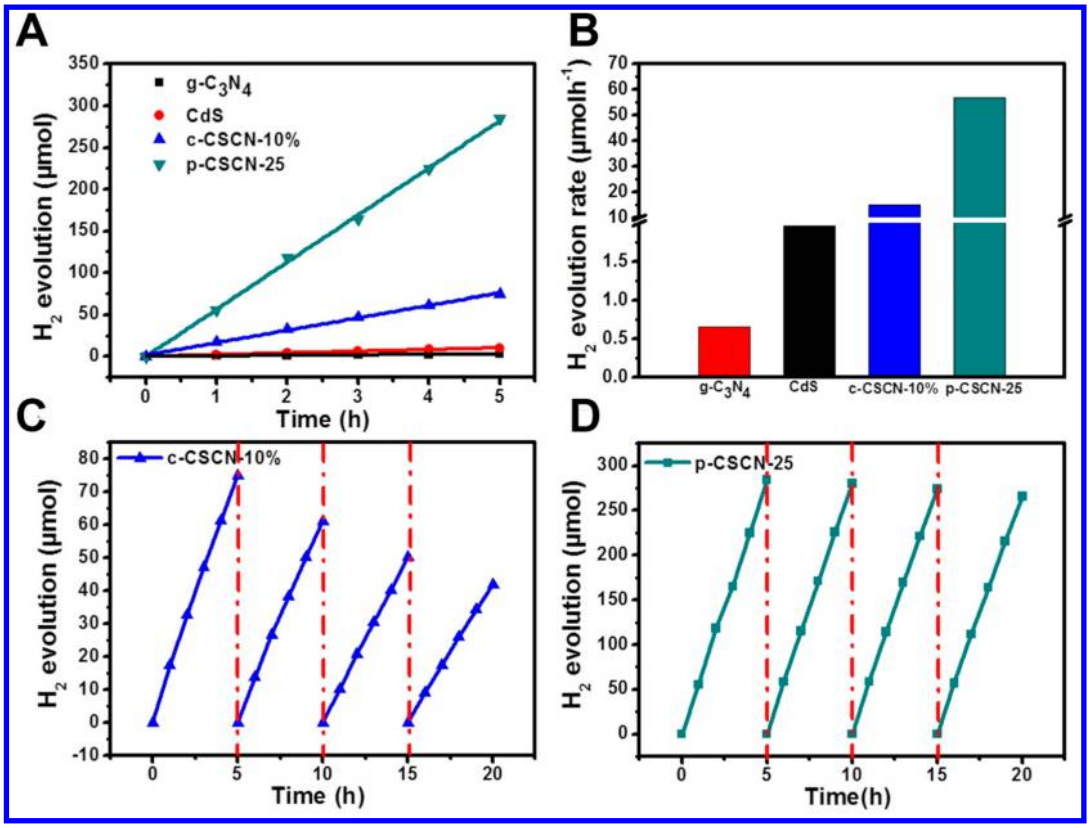


**Figure 4.** Photocatalytic performance of g-$C_3N_4$, CdS, c-CSCN-10%, and p-CSCN-25 and the composite photocatalyst stabilities. (A) Amount of $H_2$ generation of g-$C_3N_4$, CdS, c-CSCN-25, and p-CSCN-10% under visible light ($\lambda$ >420 nm) for 25 mg of the photocatalyst in 0.05 M $Na_2S$−0.1 M $Na_2SO_3$ aqueous solution for 5 h. (B) Their photocatalytic $H_2$ production rate. Cycling test of photocatalytic $H_2$ evolution for c-CSCN-10% (C) and p-CSCN-25 (D) composites with 1.0 wt % cocatalyst Pt nanoparticles. Conditions: light source, 300 W Xe lamp, $\lambda$ >420 nm; reaction solution, 100 mL of $Na_2S$ (0.05 mol/L)−$Na_2SO_3$ (0.1 mol/L) aqueous solution aqueous solution; catalyst 25 mg.

site of $PbO_2$ nanoparticles, where the $Pb^{2+}$ is oxidized by holes and forms $PbO_2$. However, the Pt nanoparticles with a lattice fringe spacing of 0.222 nm grow together with CdS nanoparticles (0.331 nm of lattice fringe space) (Figure 3D,H), implying that the electron transfers from CdS to Pt nanoparticles. In the case of p-CSCN, the photogenerated electron will be transferred from g-$C_3N_4$ to CdS and the hole remains at g-$C_3N_4$. These charge tracking results manifested that the photogenerated charge has entirely different transfer routes for c-CSCN and p-CSCN samples.

On the basis of the PL and charge tracking results, c-CSCN forms a Z-scheme type photocatalyst and p-CSCN is a type II heterojunction photocatalyst. The charge transfer directions are also displayed in Figure 1E,F.

To further confirm our proposal, photocatalytic performance and stability were investigated. $H_2$ production is a typical method to characterize the photocatalytic activity of a catalyst. As is well-known, $Na_2S$−$Na_2SO_3$ buffer solution is a common sacrificial agent for $H_2$ production for sulfide type photocatalysts to depress photocorrosion. Figure 4A,B exhibits the photocatalytic activities of g-$C_3N_4$, CdS, c-CSCN, and p-CSCN loaded with 1.0 wt % Pt nanoparticles in a $Na_2S$−$Na_2SO_3$ buffer solution, respectively. A 25 mg portion of g-$C_3N_4$ exhibits weak photocatalytic activity (0.65 $\mu$mol $h^{-1}$) under visible light irradiation ($\lambda$ >420 nm). For comparison, CdS prepared from a hydrothermal route shows the photocatalytic $H_2$ evolution rate of 1.96 $\mu$mol $h^{-1}$ for 25 mg of the photocatalyst. c-CSCN-10% shows a photocatalytic activity of 14.9 $\mu$mol $h^{-1}$, which is higher than that of any single component. In the case of p-CSCN-25, the photocatalytic rate reaches 56.9 $\mu$mol $h^{-1}$, which is the highest among these samples. Figure 4C,D illustrates the durability of c-CSCN-10% and p-CSCN-25 samples. The stability of c-CSCN-10% and p-CSCN-25 was tested in $Na_2S$−$Na_2SO_3$ buffer solution for four times of repeated photocatalytic $H_2$ production. After four recycles, c-CSCN-10% had a serious loss of activity (~50%), implying that the catalyst c-CSCN-10% was photocorroded during the $H_2$ production. Normally, photocorrosion happens due to the sulfide being oxidized by holes. It can be depressed by rapidly transferring the holes away from the sulfide. In contrast, p-CSCN-25 showed much better stability during the photocatalytic $H_2$ evolution. This is a clear sign that holes are transferred away from the sulfide. To confirm this speculation, triethanolamine (TEOA) was also used as a sacrificial agent to test the photocatalytic activity and stability, as shown in Figure S9. CdS exhibits worse stability in the first 5 h test in comparison to that in the $Na_2S$−$Na_2SO_3$ buffer solution due to photocorrosion. Although the photocatalytic activities of c-CSCN-10% and p-CSCN-25 are lower than those in the $Na_2S$−$Na_2SO_3$ system, p-CSCN-25 still exhibits the best photocatalytic activity and excellent stability among all the samples. Since p-CSCN shows super stability, this is strong evidence that the hole might be transferred away from the CdS site.

On the basis of the UV−vis spectra (Figure S2), although the c-CSCN shows broader light absorption, the overall photocatalytic activity of c-CSCN is worse than that of p-CSCN. To understand these results, the wavelength dependence of the $H_2$ evolution rate was investigated for c-CSCN and p-CSCN.


DOI: 10.1021/acscatal.7b04323
ACS Catal. 2018, 8, 2209−2217

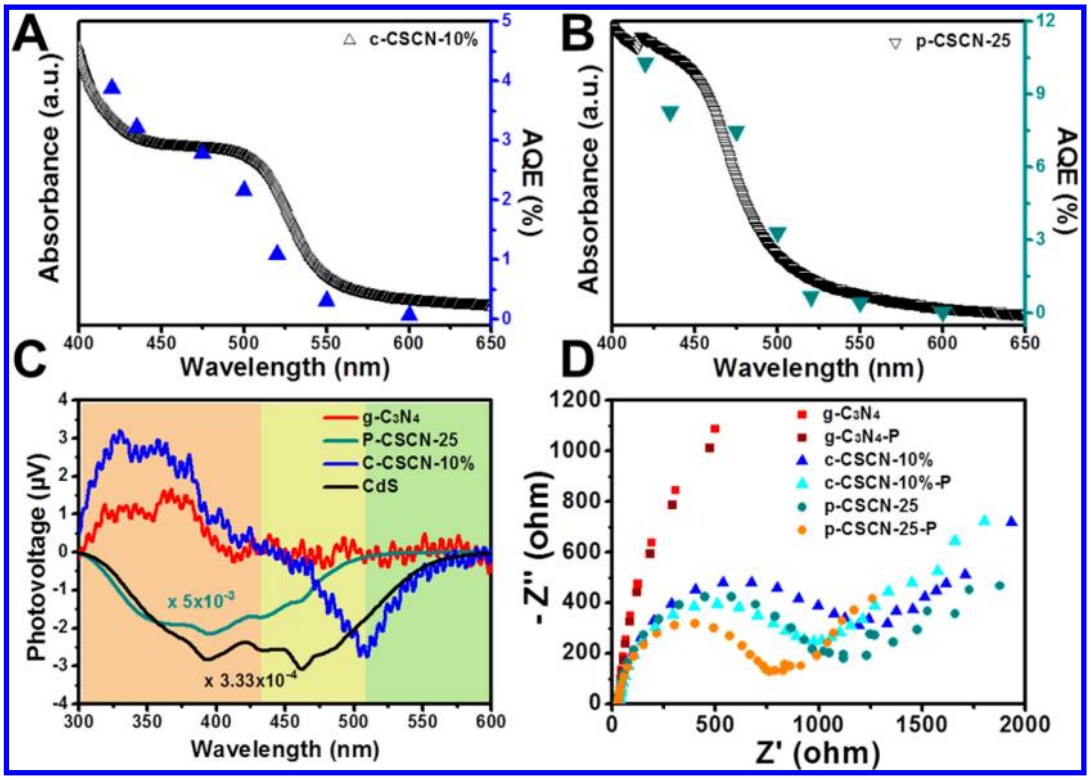


**Figure 5.** Apparent quantum efficiency and UV−vis spectra of c-CSCN (A) and p-CSCN (B). (C) Surface photovoltage spectra of g-$C_3N_4$, CdS, p-CSCN-25, and c-CSCN-10%. The signal intensity of CdS and p-CSCN-25 was divided by 3000 and 200 to fit into the plot. (D) Electrochemical impedance spectroscopy (EIS) of g-$C_3N_4$, c-CSCN, and p-CSCN with/without light irradiation (P).

Figure 5A,B shows the apparent quantum efficiency (AQE) vs wavelength plot together with the UV−vis absorption spectra of c-CSCN-10% and p-CSCN-25, respectively. In both cases, the change in AQE follows the change in absorption spectra. For the c-CSCN-10% sample, the AQE is about 3.8% at 420 nm, reaches a plateau in the range from 430 to 500 nm, and then decreases quickly to 0.3% at 550 nm. In the case of p-CSCN-25, the AQE is about 10.3% at 420 nm, which is much higher than that of c-CSCN, and the AQE maintains a short plateau from 430 to ∼475 nm (>7.5%) and then quickly decreases to 0.7% at 520 nm. The AQE trend fully matches with the light absorption in both cases. However, AQE indicates that the light conversion efficiency of p-CSCN is higher than that of c-CSCN. When photocatalytic activity and light absorption are considered, it is possible that the charge separation efficiency in p-CSCN is much better than that in c-CSCN.

To investigate the charge transfer efficiency, the surface photovoltage spectroscopy (SPS) of CdS/g-$C_3N_4$ composite nanosheets was investigated in comparison with those of pure g-$C_3N_4$ and CdS. As shown in Figure 5C, a poor response appears on the SPS curve of pure g-$C_3N_4$ nanosheets, indicating very low efficiency in the photovoltaic conversion. It shows an obvious positive photovoltage response in the range of 300−440 nm for pure g-$C_3N_4$, which is the typical feature of an n-type semiconductor.[38,42,43] The low photovoltage of g-$C_3N_4$ can be attributed to the Schottky interface contact between g-$C_3N_4$ and ITO glass in the absence of electrolyte, which leads to a limited electron transfer process from g-$C_3N_4$ to the ITO glass electrode. In contrast, CdS exhibited relatively strong negative SPS response, whose intensity was divided by 3000, corresponding to the high charge separation rate.[44] A negative photovoltage signal indicates electron transfer toward the metal substrate. Its photovoltage response fully matches with its UV−vis spectrum ranging from 300 to 600 nm. After loading with CdS on g-$C_3N_4$, the SPS signals of composites are stronger than that of g-$C_3N_4$, indicating the charge separation of composites is more efficient than that of g-$C_3N_4$. In the case of p-CSCN, the photogenerated electron transfers from g-$C_3N_4$ to CdS due to the formation of a type II heterojunction; thus, the SPS signal is negative, which is similar to the signal of CdS. In the case of c-CSCN, the SPS signal covers from 300 to 600 nm because CdS has broader light adsorption in c-CSCN. The negative SPS signal is observed in the long-wavelength region because g-$C_3N_4$ has no absorption and only CdS absorbs light in this region. In the middle-wavelength region, a weak light adsorption from defects of g-$C_3N_4$ (positive signal) and light absorption from CdS (negative signal) lead to the decreased signal of CdS. With the light absorption enhancement of g-$C_3N_4$, the formation of a Z-scheme species results in more electrons being kept at the g-$C_3N_4$; thus, the SPS signal turns positive, which is similar to the case for pure g-$C_3N_4$. For p-CSCN, the photovoltage response starts from 300 to 480 nm and is negative, which means that the electrons stay on the CdS and follow the behavior of pure CdS. It should be noted that the SPS signal was divided by 200 in order to fit into the plot. This indicates that the charge separation efficiency is much better than those of g-$C_3N_4$ and c-CSCN.

Furthermore, transient photocurrents of samples were measured during repeated ON/OFF illumination cycles at 0.2 V bias voltage. All samples exhibit reproducible photocurrent response on each illumination (Figure S10). When the light was on, the photocurrent rapidly jumped up and reached a stable value, and the photocurrent dropped to the baseline


DOI: 10.1021/acscatal.7b04323
ACS Catal. 2018, 8, 2209−2217

when the irradiation was interrupted. The transient photocurrent density of p-CSCN-25 is more than 0.64 $\mu$A cm$^{-2}$, whereas those of c-CSCN-10% and g-$C_3N_4$ are ~0.4 and 0.24 $\mu$A cm$^{-2}$, respectively. The photocurrent density of p-CSCN is larger than those of c-CSCN and g-$C_3N_4$. These results confirm that composite photocatalysts have better charge separation efficiency in comparison to g-$C_3N_4$ and that p-CSCN has better charge separation efficiency in comparison to c-CSCN.

It is commonly known that electrochemical impedance spectroscopy (EIS) analysis provides information about the interfacial properties of electrodes. The diameter of the semicircle in EIS is related to the electron transfer resistance, which brings out electron transfer kinetics of the redox probe at the electrode/electrolyte interface. In the equivalent circuit (Figure S11), $R_s$ is the series resistance, CPE is the constant phase element for the electrolyte/electrode interface, and $R_p$ is the charge transfer resistance across the electrode/electrolyte interface. In general, the smaller the radius of the semicircle, the smaller the charge transfer resistance, denoting faster separation and transfer of the photogenerated electron−hole pairs.[45] As shown in Figure 5D, the large arc radius of pure g-$C_3N_4$ may be caused by poor electrical conductivity and high resistance of the C−N network. The radius of the semicircles decreases significantly after incorporation of the CdS particles. The $R_p$ value dramatically decreases from 3260 to 1030 Ω for c-CSCN-10% and 793 Ω for p-CSCN-25, respectively. These confirm that the p-CSCN-25 has best charge transfer efficiency. Under light irradiation, the radius of the semicircle turns smaller in comparison with dark cases. This indicates that the light irradiation will enhance the charge separation and transfer. On the basis of the above results, although p-CSCN has narrower light adsorption, it has a more efficient charge separation process in compariso to c-CSCN. This is the reason p-CSCN has better $H_2$ production activity.

Although both c-CSCN and p-CSCN have the same composition of CdS and g-$C_3N_4$, they build up different types of composites, a type II heterojunction and Z-scheme, due to the different synthesis routea. For p-CSCN, the photodeposition is a light-induced reduction reaction and the CdS is grown at an active site at which an electron is ready to transfer onto g-$C_3N_4$. This is why p-CSCN tends to transfer electrons from g-$C_3N_4$. Thus, by regulating the electron flow direction, we can a construct heterojunction type photocatalyst. In the case of c-CSCN, the chemical deposition sites of CdS are randomly dispersed on g-$C_3N_4$, because it is in the reaction solution. The electron from g-$C_3N_4$ does not prefer to flow toward CdS. The excited electron of CdS has a great opportunity to combine with the hole of g-$C_3N_4$ and create the Z-scheme type catalyst. In this report, we start from g-$C_3N_4$ (PSII) and deposit CdS (PSI) via a photoreduction reaction, and a type II heterojunction catalyst is obtained. If we start from PSII and deposit PSI via a photo-oxidation reaction, a Z-scheme type catalyst will be formed.

## CONCLUSIONS

In summary, we built up two composites from CdS and g-$C_3N_4$ via photodeposition and chemical hydrothermal routes. These two composites exhibit different photocatalytic activities and stabilities. From tracking of the charge flow direction and PL spectroscopy, the electron tends to transfer from g-$C_3N_4$ to CdS and the hole goes to g-$C_3N_4$ to form a type II heterojunction in the case of p-CSCN. In contrast, the electron tends to remain at g-$C_3N_4$ and the hole stays at CdS and creates a direct Z-scheme species. SPS spectra, EIS spectroscopy, and AQE results indicate that the charge separation of p-CSCN is more efficient than that of c-CSCN in the CdS/g-$C_3N_4$ composites. For an analysis of the reason, p-CSCN was synthesized from photodeposition of CdS on g-$C_3N_4$, which is a photogenerated electron induced reduction reaction on the surface of g-$C_3N_4$. This indicates that the photogenerated electron highly prefers to flow from g-$C_3N_4$ to CdS. However, as c-CSCN is produced by chemical reduction deposition, there no preferred site for the photogenerated electron. These results demonstrated that photodeposition could be used for the regulation of photogenerated charge flow direction. Furthermore, it can be used for constructing a direct Z-scheme and/or type II heterojunction. This report may open the door to regulate Z-scheme and type II heterojunction and judge the composite form as being a type II heterojunction or Z-scheme.

## EXPERIMENTAL SECTION

**Synthesis of the Photocatalysts.** All chemicals were analytical grade and were used without further purification.

*Preparation of g-$C_3N_4$.*[30] Graphitic carbon nitride (g-$C_3N_4$) powder was synthesized by the pyrolysis of urea. A 50 g portion of urea was put into an alumina crucible with a cover and then heated to 550 °C for 3 h in a muffle furnace at a temperature rate of 0.5 °C/min.

*Preparation of Photodeposited CdS/g-$C_3N_4$ (p-CSCN).*[46] The sample of p-CSCN was prepared by photodeposition. Sulfur (2 mmol) and $Cd(NO_3)_2{\cdot}4H_2O$ (8 mmol) were added to 200 mL of an ethanol suspension containing 200 mg of g-$C_3N_4$. This suspension was irradiated with a 300 W Xe lamp for 5 h under different temperatures of circulating water. Then the solid product was collected by centrifugation and washed several times with deionized water, ethanol, and carbon disulfide ($CS_2$) to remove unreacted raw materials such $Cd(NO_3)_2$ and S powder. The samples produced at temperatures of 4, 25, and 50 °C were dried in the oven at 60 °C overnight and denoted p-CSCN-4, p-CSCN-25, p-CSCN-50, respectively.

*Preparation of Chemical-Deposited CdS/g-$C_3N_4$ (c-CSCN).*[32] The sample of c-CSCN was produced by chemical deposition. A 0.35 mmol portion of $Cd(NO_3)_2{\cdot}4H_2O$ and 1.503 g of thioacetamide (TAA) were added to 60 mL of deionized water containing 0.5 g of as-prepared g-$C_3N_4$. The achieved suspension was ultrasonicated for 30 min and subsequently transferred into a 100 mL Teflon-lined stainless steel autoclave, and then it was heated to 160 °C and kept at this temperature for 5 h. The obtained sample was washed several times with deionized water and ethanol, dried in the oven at 60 °C, and denoted by c-CSCN-10%. The others c-CSCN samples were synthesized by a similar method by changing the amount of $Cd(NO_3)_2{\cdot}4H_2O$. These samples according to the weight ratio of g-$C_3N_4$ and CdS are denoted c-CSCN-1% (0.035 mmol of $Cd(NO_3)_2{\cdot}4H_2O$), c-CSCN-5% (0.175 mmol of $Cd(NO_3)_2{\cdot}4H_2O$), c-CSCN-10% (0.35 mmol of $Cd(NO_3)_2{\cdot}4H_2O$), and c-CSCN-15% (0.525 mmol of $Cd(NO_3)_2{\cdot}4H_2O$), respectively. The pure CdS photocatalyst was obtained under the same conditions without adding g-$C_3N_4$ powder.

**Characterizations.** The crystal structures of the samples were investigated using X-ray diffraction (XRD; Bruker D8 Advance X-ray diffractometer) with Cu K$\alpha$ radiation ($\lambda$ = 0.15406 nm) as the incident beam at 40 kV and 40 mA. The morphologies of the samples were examined by transmission


DOI: 10.1021/acscatal.7b04323
ACS Catal. 2018, 8, 2209−2217

electron microscopy (TEM; FEI Tecnai G2 F20) operated at 200 kV and scanning electron microscopy (SEM; JEOL S-4800) operated at 5 kV. UV−vis diffuse reflection spectroscopy (DRS) was performed on a Shimadzu UV-2600 spectrophotometer using $BaSO_4$ as the reference. The photoluminescence (PL) spectra of the photocatalyst were obtained by a Hitachi F-7000 instrument with an excitation wavelength of 325 nm. The BET specific surface area was measured using a Quantachrome Surface Area and Pore Size Analyzer (Quantachrome Instruments version 3.01). Electrochemical measurements were conducted with an Autolab PGSTAT302N instrument in a conventional three-electrode cell, using a carbon electrode as the counter electrode and an Ag/AgCl electrode as the reference electrode. The working electrode[47] was prepared on FTO glass that had been cleaned by sonication in ethanol for 30 min and dried at 100 °C. The 20 mg of the sample was dispersed in 100 mL of a 0.2 mg $mL^{-1}$ $I_2$/acetone solution under ultrasonic treatment. A two-electrode process was used to deposit the samples at an applied potential of 10 V for 3 min. FTO glass substrates with a coated area of about 1 × 1 $cm^2$ were used for both electrodes. Then, the deposited electrode was dried at 300 °C for 60 min to remove residual $I_2$.

**Photocatalytic Hydrogen Evolution.** Photocatalytic hydrogen evolution via water splitting was performed in a closed Pyrex glass reactor. For investigations of photocatalytic performance, the well-ground photocatalyst (10 mg) was suspended in $Na_2S$ (0.05 M) and $Na_2SO_3$ (0.1 M) aqueous solution (100 mL) under vigorous stirring. A 1 wt % amount of Pt was photodeposited onto the catalysts using $H_2PtCl_6$ dissolved in the reactant solution. A 300 W Xe lamp was also utilized as the visible light source for irradiation with a 420 nm cutoff filter for the photocatalytic reactions. The temperature of the reactant solution was maintained at 0 °C by a flow of a cycle cooling water system during the reaction. The amount of hydrogen produced was determined by gas chromatography (Shimadzu GC-2014C), using a thermal conductivity detector (TCD) with $N_2$ as the carrier gas. Wavelength-dependent $H_2$ evolution measurement was also operated in the $H_2$ production system with band-pass filters for 420, 435, 475, 500, 520, 550, and 600 nm, respectively. The apparent quantum efficiency (AQE) was estimated using the equation

$$\text{AQE}\ (\%) = \frac{2 \times \text{number of evolved } H_2 \text{ molecules}}{\text{number of incident photons}} \times 100\%$$

The stability tests of the as-prepared composite materials (25 mg) of p-CSCN-25 and c-CSCN-10% were operated in the $H_2$ production system using $Na_2S$ (0.05 M)/$Na_2SO_3$ (0.1 M) aqueous solution and 10 vol % triethanolamine (TEOA) aqueous solution as an electron donor.

**Charge Flow Tracking by Photodeposition.**[48] Photodeposition of 1 wt % Pt and $PbO_2$ on the surfaces of p-CSCN-25 (c-CSCN-10%) were carried out using $H_2PtCl_6$ and $Pb(NO_3)_2$ as precursors, respectively. Typically, 10 mg of p-CSCN-25 (c-CSCN-10%) and a calculated amount of the metal precursor were mixed in 100 mL of deionized water with stirring. The suspension was then irradiated by a 300 W Xe lamp with the reaction temperature maintained at 0 °C by cycle cooling water equipment. After 2 h of photodeposition, the suspension was filtered, washed several times with deionized water, and finally dried in the oven at 60 °C overnight. For photodeposition of Pt and $PbO_2$, $Na_2S$/$Na_2SO_3$ (molar ratio of 1/2) aqueous solution and 0.1 M $NaIO_3$ aqueous solution were used as electron donors and acceptors, respectively.

## ■ ASSOCIATED CONTENT

### Supporting Information

The Supporting Information is available free of charge on the ACS Publications website at DOI: 10.1021/acscatal.7b04323.

Optical photography, UV−vis, TEM, XRD, $H_2$ production, $N_2$ sorption, SEM, photocurrent and electrochemical impedance spectroscopy (PDF)

## ■ AUTHOR INFORMATION


### Corresponding Author

*E-mail for Z.S.: sunzc@bjut.edu.cn.

### ORCID

Franklin Feng Tao: 0000-0002-4916-6509

Zaicheng Sun: 0000-0002-7059-3177


### Notes

The authors declare no competing financial interest.

## ■ ACKNOWLEDGMENTS

Z.S. thanks the financial support from the National Natural Science Foundation of China (21671011), Beijing High Talent Program and Beijing Natural Science Foundation (KZ201710005002), Beijing Municipal High Level Innovative Team Building Program (IDHT20180504), Large-scale Instrument and Equipment Platform of Beijing University of Technology. The authors thank China Postdoctoral Science Foundation and Beijing Postdoctoral Research Foundation.

## ■ REFERENCES


(1) Chen, X.; Shen, S.; Guo, L.; Mao, S. S. Semiconductor-Based Photocatalytic Hydrogen Generation. *Chem. Rev.* **2010**, *110*, 6503−6570.

(2) Kudo, A.; Miseki, Y. Heterogeneous Photocatalyst Materials for Water Splitting. *Chem. Soc. Rev.* **2009**, *38*, 253−278.

(3) Maeda, K.; Teramura, K.; Lu, D.; Takata, T.; Saito, N.; Inoue, Y.; Domen, K. Photocatalyst Releasing Hydrogen from Water. *Nature* **2006**, *440*, 295−295.

(4) Kundu, S.; Patra, A. Nanoscale Strategies for Light Harvesting. *Chem. Rev.* **2017**, *117*, 712−757.

(5) Ong, W.-J.; Tan, L.-L.; Ng, Y. H.; Yong, S.-T.; Chai, S.-P. Graphitic Carbon Nitride ($g\text{-}C_3N_4$)-Based Photocatalysts for Artificial Photosynthesis and Environmental Remediation: Are We a Step Closer to Achieving Sustainability? *Chem. Rev.* **2016**, *116*, 7159−7329.

(6) Wang, H.; Zhang, L.; Chen, Z.; Hu, J.; Li, S.; Wang, Z.; Liu, J.; Wang, X. Semiconductor Heterojunction Photocatalysts: Design, Construction, and Photocatalytic Performances. *Chem. Soc. Rev.* **2014**, *43*, 5234−5244.

(7) Zhang, P.; Wang, T.; Chang, X.; Gong, J. Effective Charge Carrier Utilization in Photocatalytic Conversions. *Acc. Chem. Res.* **2016**, *49*, 911−921.

(8) Zhao, Y.; Zhao, B.; Liu, J.; Chen, G.; Gao, R.; Yao, S.; Li, M.; Zhang, Q.; Gu, L.; Xie, J. Oxide-Modified Nickel Photocatalysts for the Production of Hydrocarbons in Visible Light. *Angew. Chem., Int. Ed.* **2016**, *55*, 4215−4219.

(9) Chen, J.; Zhao, D.; Diao, Z.; Wang, M.; Shen, S. Ferrites Boosting Photocatalytic Hydrogen Evolution over Graphitic Carbon Nitride: a Case Study of (Co, Ni) $Fe_2O_4$ Modification. *Sci. Bull.* **2016**, *61*, 292−301.

(10) Yu, H.; Shi, R.; Zhao, Y.; Bian, T.; Zhao, Y.; Zhou, C.; Waterhouse, G. I. N.; Wu, L.-Z.; Tung, C.-H.; Zhang, T. Alkali-Assisted Synthesis of Nitrogen Deficient Graphitic Carbon Nitride




DOI: 10.1021/acscatal.7b04323
*ACS Catal.* 2018, 8, 2209−2217

with Tunable Band Structures for Efficient Visible-Light-Driven Hydrogen Evolution. *Adv. Mater.* **2017**, *29*, 1605148.
(11) Martin, D. J.; Qiu, K.; Shevlin, S. A.; Handoko, A. D.; Chen, X.; Guo, Z.; Tang, J. Highly Efficient Photocatalytic $H_2$ Evolution from Water Using Visible Light and Structure-Controlled Graphitic Carbon Nitride. *Angew. Chem., Int. Ed.* **2014**, *53*, 9240−9245.
(12) Banerjee, S.; Mohapatra, S. K.; Das, P. P.; Misra, M. Synthesis of Coupled Semiconductor by Filling 1D $TiO_2$ Nanotubes with CdS. *Chem. Mater.* **2008**, *20*, 6784−6791.
(13) Jang, J. S.; Choi, S. H.; Kim, H. G.; Lee, J. S. Location and State of Pt in Platinized CdS/$TiO_2$ Photocatalysts for Hydrogen Production from Water under Visible Light. *J. Phys. Chem. C* **2008**, *112*, 17200−17205.
(14) Low, J.; Yu, J.; Jaroniec, M.; Wageh, S.; Al-Ghamdi, A. A. Heterojunction Photocatalysts. *Adv. Mater.* **2017**, *29*, 1601694.
(15) Farquhar, G. D.; Sharkey, T. D. Stomatal Conductance and Photosynthesis. *Annu. Rev. Plant Physiol.* **1982**, *33*, 317−345.
(16) Jiang, C.; Moniz, S. J.; Wang, A.; Zhang, T.; Tang, J. Photoelectrochemical Devices for Solar Water Splitting−Materials and Challenges. *Chem. Soc. Rev.* **2017**, *46*, 4645−4660.
(17) Abe, R.; Sayama, K.; Domen, K.; Arakawa, H. A New Type of Water Splitting System Composed of Two Different $TiO_2$ Photocatalysts (Anatase, Rutile) and a $IO_3^-/I^-$ Shuttle Redox Mediator. *Chem. Phys. Lett.* **2001**, *344*, 339−344.
(18) Maeda, K.; Higashi, M.; Lu, D.; Abe, R.; Domen, K. Efficient Nonsacrificial Water Splitting through Two-Step Photoexcitation by Visible Light Using a Modified Oxynitride as a Hydrogen Evolution Photocatalyst. *J. Am. Chem. Soc.* **2010**, *132*, 5858−5868.
(19) Sasaki, Y.; Kato, H.; Kudo, A. $[Co(bpy)_3]^{3+/2+}$ and $[Co(phen)_3]^{3+/2+}$ Electron Mediators for Overall Water Splitting under Sunlight Irradiation Using Z-scheme Photocatalyst System. *J. Am. Chem. Soc.* **2013**, *135*, 5441−5449.
(20) Tada, H.; Mitsui, T.; Kiyonaga, T.; Akita, T.; Tanaka, K. All-Solid-State Z-scheme in CdS−Au−$TiO_2$ Three-Component Nanojunction System. *Nat. Mater.* **2006**, *5*, 782−786.
(21) Iwase, A.; Ng, Y. H.; Ishiguro, Y.; Kudo, A.; Amal, R. Reduced Graphene Oxide as A Solid-State Electron Mediator in Z-Scheme Photocatalytic Water Splitting under Visible Light. *J. Am. Chem. Soc.* **2011**, *133*, 11054−11057.
(22) Ye, L.; Liu, J.; Gong, C.; Tian, L.; Peng, T.; Zan, L. Two Different Roles of Metallic Ag on Ag/AgX/BiOX (X= Cl, Br) Visible Light Photocatalysts: Surface Plasmon Resonance and Z-Scheme Bridge. *ACS Catal.* **2012**, *2*, 1677−1683.
(23) Maeda, K. Z-scheme Water Splitting Using Two Different Semiconductor Photocatalysts. *ACS Catal.* **2013**, *3*, 1486−1503.
(24) Zhou, P.; Yu, J.; Jaroniec, M. All-Solid-State Z-Scheme Photocatalytic Systems. *Adv. Mater.* **2014**, *26*, 4920−4935.
(25) Majek, M.; Jacobi von Wangelin, A. Mechanistic Perspectives on Organic Photoredox Catalysis for Aromatic Substitutions. *Acc. Chem. Res.* **2016**, *49*, 2316−2327.
(26) Low, J.; Jiang, C.; Cheng, B.; Wageh, S.; Al-Ghamdi, A. A.; Yu, J. A Review of Direct Z-Scheme Photocatalysts. *Small Methods* **2017**, *1*, 1700080.
(27) Zhang, L. J.; Li, S.; Liu, B. K.; Wang, D. J.; Xie, T. F. Highly Efficient CdS/$WO_3$ Photocatalysts: Z-Scheme Photocatalytic Mechanism for Their Enhanced Photocatalytic $H_2$ Evolution under Visible Light. *ACS Catal.* **2014**, *4*, 3724−3729.
(28) Maeda, K.; Lu, D.; Domen, K. Solar-Driven Z-scheme water splitting using modified $BaZrO_3$−$BaTaO_2N$ solid solutions as photocatalysts. *ACS Catal.* **2013**, *3*, 1026−1033.
(29) Wenderich, K.; Mul, G. Methods, Mechanism, and Applications of Photodeposition in Photocatalysis: A Review. *Chem. Rev.* **2016**, *116*, 14587−14619.
(30) Liu, J.; Zhang, T.; Wang, Z.; Dawson, G.; Chen, W. Simple Pyrolysis of Urea into Graphitic Carbon Nitride with Recyclable Adsorption and Photocatalytic Activity. *J. Mater. Chem.* **2011**, *21*, 14398−14401.
(31) Yun, H. J.; Lee, H.; Kim, N. D.; Lee, D. M.; Yu, S.; Yi, J. A Combination of Two Visible-Light Responsive Photocatalysts for Achieving the Z-Scheme in the Solid State. *ACS Nano* **2011**, *5*, 4084−4090.
(32) Dai, X.; Xie, M.; Meng, S.; Fu, X.; Chen, S. Coupled Systems for Selective Oxidation of Aromatic Alcohols to Aldehydes and Reduction of Nitrobenzene into Aniline Using CdS/g-$C_3N_4$ Photocatalyst under Visible Light Irradiation. *Appl. Catal., B* **2014**, *158-159*, 382−390.
(33) Zhao, W.-W.; Wang, J.; Xu, J.-J.; Chen, H.-Y. Energy Transfer between CdS Quantum Dots and Au Nanoparticles in Photoelectrochemical Detection. *Chem. Commun.* **2011**, *47*, 10990−10992.
(34) Xu, Y.; Schoonen, M. A. A. The Absolute Energy Positions of Conduction and Valence Bands of Selected Semiconducting Minerals. *Am. Mineral.* **2000**, *85*, 543−556.
(35) Jin, J.; Yu, J.; Guo, D.; Cui, C.; Ho, W. A Hierarchical Z-Scheme CdS−$WO_3$ Photocatalyst with Enhanced $CO_2$ Reduction Activity. *Small* **2015**, *11*, 5262−5271.
(36) Wang, X.; Maeda, K.; Thomas, A.; Takanabe, K.; Xin, G.; Carlsson, J. M.; Domen, K.; Antonietti, M. A Metal-Free Polymeric Photocatalyst for Hydrogen Production from Water under Visible Light. *Nat. Mater.* **2009**, *8*, 76−80.
(37) Yan, H.; Huang, Y. Polymer Composites of Carbon Nitride and Poly (3-Hexylthiophene) to Achieve Enhanced Hydrogen Production from Water under Visible Light. *Chem. Commun.* **2011**, *47*, 4168−4170.
(38) Bai, X.; Sun, C.; Wu, S.; Zhu, Y. Enhancement of Photocatalytic Performance via a P3HT-g-$C_3N_4$ Heterojunction. *J. Mater. Chem. A* **2015**, *3*, 2741−2747.
(39) Ge, L.; Zuo, F.; Liu, J.; Ma, Q.; Wang, C.; Sun, D.; Bartels, L.; Feng, P. Synthesis and Efficient Visible Light Photocatalytic Hydrogen Evolution of Polymeric g-$C_3N_4$ Coupled with CdS Quantum Dots. *J. Phys. Chem. C* **2012**, *116*, 13708−13714.
(40) Tu, W.; Zhou, Y.; Feng, S.; Xu, Q.; Li, P.; Wang, X.; Xiao, M.; Zou, Z. Hollow Spheres Consisting of $Ti_{0.91}O_2$/CdS Nanohybrids for $CO_2$ Photofixation. *Chem. Commun.* **2015**, *51*, 13354−13357.
(41) Li, R.; Zhang, F.; Wang, D.; Yang, J.; Li, M.; Zhu, J.; Zhou, X.; Han, H.; Li, C. Spatial Separation of Photogenerated Electrons and Holes among {010} and {110} Crystal Facets of $BiVO_4$. *Nat. Commun.* **2013**, *4*, 1432.
(42) Bi, L.; Xu, D.; Zhang, L.; Lin, Y.; Wang, D.; Xie, T. Metal Ni-Loaded g-$C_3N_4$ for Enhanced Photocatalytic $H_2$ Evolution Activity: the Change in Surface Band Bending. *Phys. Chem. Chem. Phys.* **2015**, *17*, 29899−29905.
(43) Raziq, F.; Qu, Y.; Zhang, X.; Humayun, M.; Wu, J.; Zada, A.; Yu, H.; Sun, X.; Jing, L. Enhanced Cocatalyst-Free Visible-Light Activities for Photocatalytic Fuel Production of g-$C_3N_4$ by Trapping Holes and Transferring Electrons. *J. Phys. Chem. C* **2016**, *120*, 98−107.
(44) Liqiang, J.; Xiaojun, S.; Jing, S.; Weimin, C.; Zili, X.; Yaoguo, D.; Honggang, F. Review of Surface Photovoltage Spectra of Nano-Sized Semiconductor and its Applications in Heterogeneous Photocatalysis. *Sol. Energy Mater. Sol. Cells* **2003**, *79*, 133−151.
(45) Hou, Y.; Laursen, A. B.; Zhang, J.; Zhang, G.; Zhu, Y.; Wang, X.; Dahl, S.; Chorkendorff, I. Layered Nanojunctions for Hydrogen-Evolution Catalysis. *Angew. Chem., Int. Ed.* **2013**, *52*, 3621−3625.
(46) Yun, H. J.; Lee, H.; Kim, N. D.; Lee, D. M.; Yu, S.; Yi, J. A Combination of Two Visible-Light Responsive Photocatalysts for Achieving the Z-Scheme in the Solid State. *ACS Nano* **2011**, *5*, 4084−4090.
(47) Zhang, G.; Sun, S.; Jiang, W.; Miao, X.; Zhao, Z.; Zhang, X.; Qu, D.; Zhang, D.; Li, D.; Sun, Z. A Novel Perovskite $SrTiO_3$-$Ba_2FeNbO_6$ Solid Solution for Visible Light Photocatalytic Hydrogen Production. *Adv. Energy Mater.* **2017**, *7*, 1600932.
(48) Wang, B.; Shen, S.; Guo, L. $SrTiO_3$ Single Crystals Enclosed with High-Indexed {023} Facets and {001} Facets for Photocatalytic Hydrogen and Oxygen Evolution. *Appl. Catal., B* **2015**, *166−167*, 320−326.


DOI: 10.1021/acscatal.7b04323
*ACS Catal.* 2018, 8, 2209−2217